iScience

CellPress
OPEN ACCESS

Article

A robust vessel-labeling pipeline with high tissue clearing compatibility for 3D mapping of vascular networks

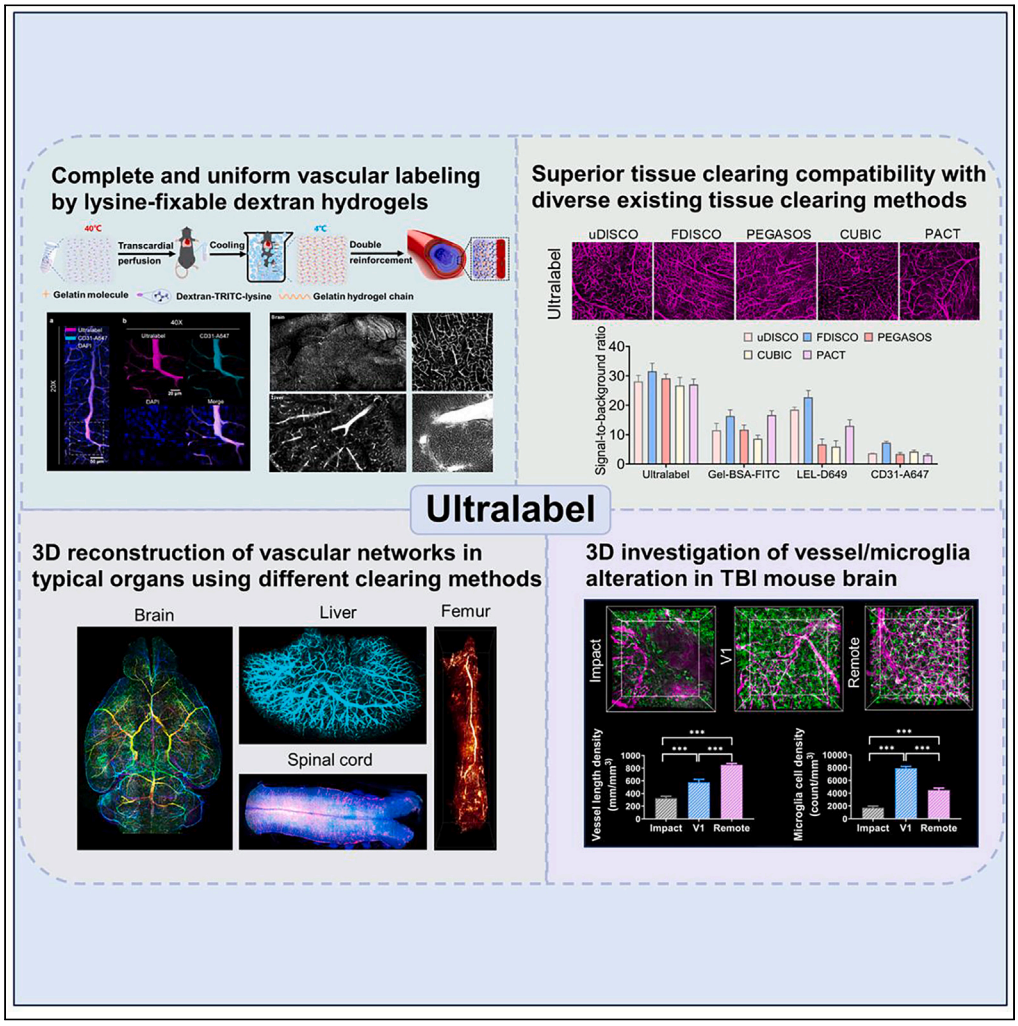

Yating Deng, Jingtan Zhu, Xiaomei Liu, Junyao Dai, Tingting Yu, Dan Zhu

yutingting@hust.edu.cn (T.Y.)
dawnzh@mail.hust.edu.cn (D.Z.)

Highlights

Ultralabel, a vessel casting method based on lysine-fixable dextran hydrogels

Ultralabel enables efficient vascular labeling for both large vessels and capillaries

Ultralabel is well compatible with diverse tissue clearing methods

Ultralabel enables 3D mapping and profiling of vascular networks in health and disease

Deng et al., iScience 27, 109730
May 17, 2024
https://doi.org/10.1016/j.isci.2024.109730

iScience

CellPress
OPEN ACCESS

Article

A robust vessel-labeling pipeline with high tissue clearing compatibility for 3D mapping of vascular networks

Yating Deng,[1,2] Jingtan Zhu,[1,2] Xiaomei Liu,[1] Junyao Dai,[1] Tingting Yu,[1,*] and Dan Zhu[1,3,*]

SUMMARY

The combination of vessel-labeling, tissue-clearing, and light-sheet imaging techniques provides a potent tool for accurately mapping vascular networks, enabling the assessment of vascular remodeling in vascular-related disorders. However, most vascular labeling methods face challenges such as inadequate labeling efficiency or poor compatibility with current tissue clearing technology, which significantly undermines the image quality. To address this limitation, we introduce a vessel-labeling pipeline, termed Ultralabel, which relies on a specially designed dye hydrogel containing lysine-fixable dextran and gelatins for double enhancement. Ultralabel demonstrates not only excellent vessel-labeling capability but also strong compatibility with all tissue clearing methods tested, which outperforms other vessel-labeling methods. Consequently, Ultralabel enables fine mapping of vascular networks in diverse organs, as well as multi-color labeling alongside other labeling techniques. Ultralabel should provide a robust and user-friendly method for obtaining 3D vascular networks in different biomedical applications.

INTRODUCTION

The intricate vascular networks within the human body play a critical role in maintaining physiological balance, not only by facilitating the efficient transport of oxygen, various nutrients, and hormones to different organs and tissues but also by aiding in the removal of metabolic waste. Disruptions in vascular structures are closely related to the development of diverse medical conditions, such as organ failure,[1,2] tumors,[3,4] and stroke.[5,6]

Due to the significance of blood vessels in clinical investigations and therapy, visualization of different vascular networks has always been a research hotspot.[7] Traditional medical imaging tomography, such as X-ray/computed tomography (CT), magnetic resonance imaging (MRI), and positron emission tomography (PET), provides powerful tools for imaging large arteries and veins in living larger animals and humans both *in vivo* and *ex vivo*.[8] In addition, recent developments in modern optical imaging techniques have made it possible for 3D imaging of vascular structures both for large vessels and small capillaries.[3] However, the imaging depth is rather limited due to the turbid nature of biological samples. To image large tissues, diverse tissue optical clearing methods have been proposed to render tissues "transparent" by overcoming tissue scattering and absorption via different physical and chemical strategies.[9–14] The combination of tissue clearing and optical imaging techniques provides an effective means to obtain the 3D structure of the vascular system.[15–17]

To obtain the fine vessel networks, efficient labeling of the entire vascular networks is the primary step highly responsible for the imaging quality.[18–21] To date, a variety of fluorescent vessel-labeling methods have been used to label the vascular structure,[22,23] which can be roughly divided into three categories. Vessel-specific marker labeling is often used instead of transgenic labeling by passive diffusion of antibodies or direct injection of fluorescent markers into the animal body. However, this kind of vessel-labeling strategy is limited by incomplete labeling, weak fluorescence signals, or incompatibility with tissue clearing. In recent years, vessel labeling via fluorescent dye filling has become famous due to its labeling completeness for both large vessels and small capillaries, as well as its high labeling efficiency and ease of handling.[16,22,24,25] However, due to the limitation of filling dyes currently used, drawbacks such as potential leakage, vessel occlusion, and weak tissue compatibility remain unresolved. There have been several recent studies trying to overcome the problem of dye leakage and vessel occlusion by using custom-made hydrogel and nanoparticles.[24,26,27] However, this will significantly raise the operation difficulty, and the tissue clearing compatibility is not obviously improved. In general, a fluorescent vessel-labeling method with both superior labeling ability and tissue clearing compatibility is still lacking.

In this study, we developed a hydrogel-based vascular labeling method, termed Ultralabel, to overcome the unresolved challenges. We used a special kind of dextran molecular dye molecule fused with lysine residue and incorporated it into gelatin hydrogel. During the vessel

[1]Britton Chance Center for Biomedical Photonics- MoE Key Laboratory for Biomedical Photonics, Advanced Biomedical Imaging Facility, Wuhan National Laboratory for Optoelectronics, Huazhong University of Science and Technology, Wuhan 430074, Hubei, China
[2]These authors contributed equally
[3]Lead contact
*Correspondence: yutingting@hust.edu.cn (T.Y.), dawnzh@mail.hust.edu.cn (D.Z.)
https://doi.org/10.1016/j.isci.2024.109730

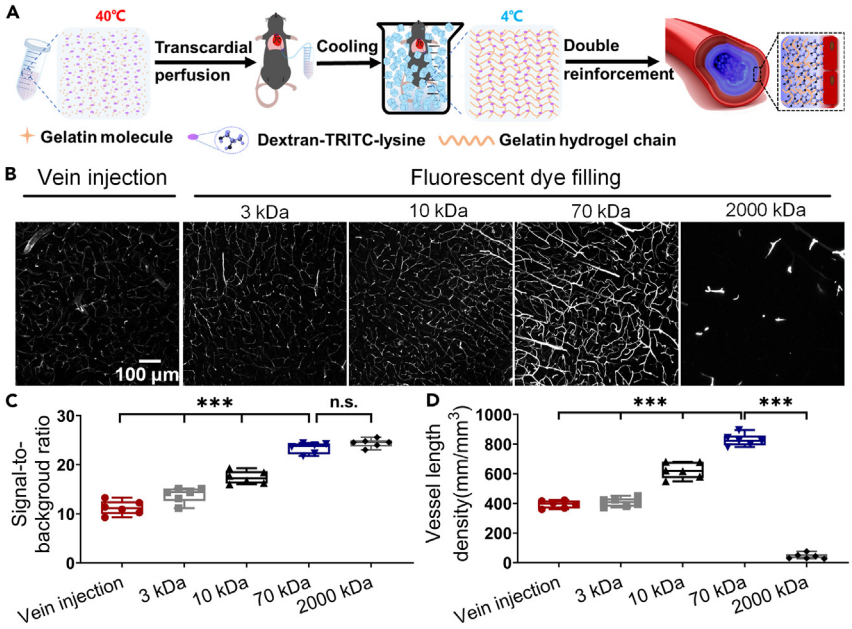

Figure 1. Overview of the Ultralabel method

(A) Principle and workflow for Ultralabel method. (The lysine-fixable dextran conjugated with tetramethylrhodamine is abbreviated as Dextran-TRITC-lysine).

(B) The labeling result via vein injection of 70 kDa Dextran-TRITC-lysine and transcardial-perfusion of hydrogel-mixed fluorescent dyes (3 kDa, 10 kDa, 70 kDa, 2,000 kDa Dextran-TRITC-lysine).

(C) The signal-to-background ratios of vascular image stacks for each labeling method ($n = 6$ samples for each group).

(D) Quantification of vessel length densities in different labeling methods ($n = 6$ samples for each group). Statistical significance in (C) and (D) (n.s., $p > 0.05$; ***, $p < 0.001$) was assessed using one-way ANOVA, followed by the Bonferroni *post hoc* test.

labeling, the dextran tracers will not only bind to the nearby endothelial cells via aldehyde-mediated fixation but also be stably entrapped in the hydrogel matrix. This double enhancement of dye molecules results in not only excellent vascular labeling performance within different organs but also unique tissue clearing compatibility better than other vessel-labeling methods tested. Using Ultralabel, we performed 3D imaging of different vascular networks within the entire organ with high quality via diverse tissue clearing methods. We believe that Ultralabel will provide powerful and robust tools for researchers to visualize the entire vascular network in numerous histological and pathological applications across the biomedical and clinical fields.

RESULTS

Development of Ultralabel protocol using hydrogel-based filling solution with lysine-fixable fluorescent dextran

We started to form the Ultralabel protocol with a dextran dye molecule covalently attached to lysine residues. Similar with the fluorescein isothiocyanate (FITC)-albumin used in previous studies,[16,24,25,28,29] this special structure facilitates the binding of dye molecules to neighboring biomolecules via aldehyde-mediated fixation and thus has the potential for robust fluorescence labeling for vasculature. As shown in Figure 1A, we combined the selected fluorescent dyes with gelatin, a hydrolysate of the natural polymer, to facilitate comprehensive labeling of vascular networks. Different from the conventional intravenous injection, filling with fluorescent hydrogels generates a complete and uniform vessel map with strengthened signal-to-background ratio (Figure 1B).

To investigate the ideal molecular weight for dextran dye molecules with lysine residues in vascular labeling, we tested four working solutions with different molecular weights (3 kDa, 10 kDa, 70 kDa, 2,000 kDa) and quantitatively evaluated their labeling performance. The vessel signals generated using 70 kDa and 2,000 kDa dyes were notably superior to those from the 3 kDa and 10 kDa dyes and the tail vein injections (Figure 1C). However, we found that the 2,000 kDa dye will result in vessel blockages and partial labeling, potentially due to its high molecular weight and weak dissolution in the gelatin solution impairing effective vascular labeling (Figure 1D). Hence, a 70 kDa dye molecule mixed with gelatin was chosen for the labeling scheme as it effectively labeled the vascular networks. This potent vessel-labeling approach has been coined "Ultralabel."

Ultralabel is applicable for labeling vascular networks of various organs with high quality

We further validated the completeness of the vascular structures formed by Ultralabel casting. Co-labeling of blood vessels using common lectin and CD31 antibodies with Ultralabel was performed. As shown, the vessels casted by Ultralabel finely covered the vascular structures stained with Lectin and CD31 antibodies (Figures 2A and 2B). However, the signal-to-background ratio of Ultralabel is significantly higher than

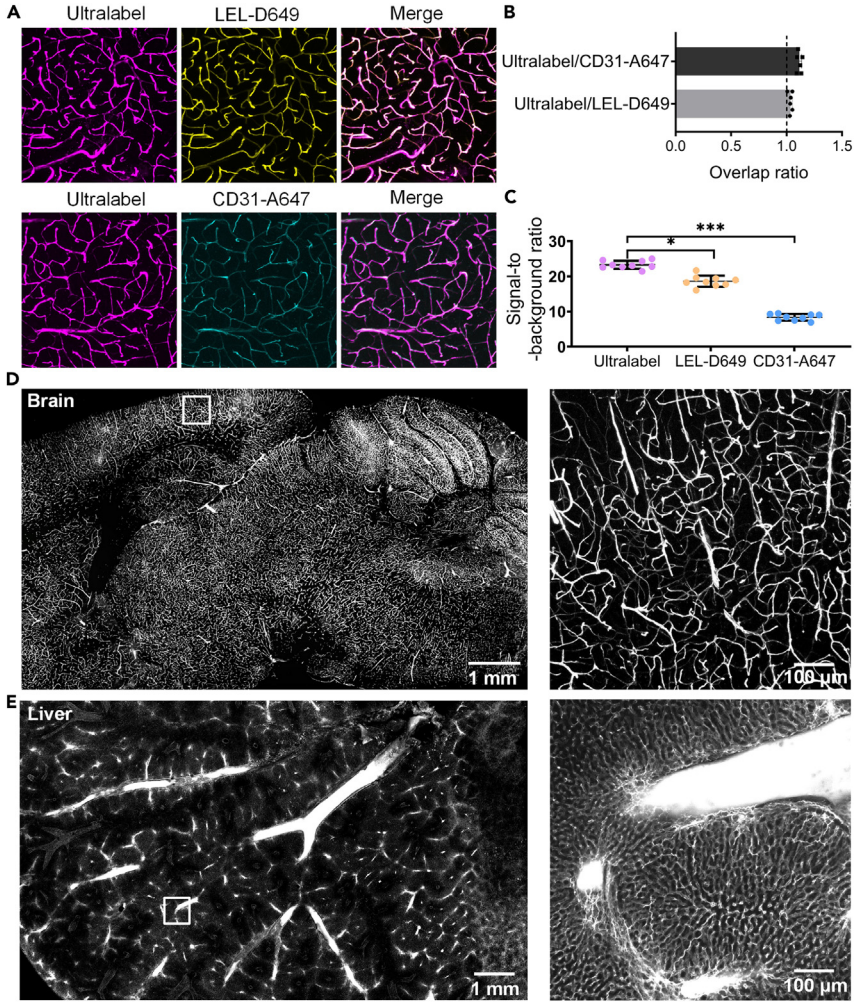

Figure 2. The Ultralabel method achieves complete and uniform labeling of blood vessels in various organs with high signal-to-background ratio

(A) Validation of labeling completeness of Ultralabel with lectin and CD31 antibodies by intravenous injection.

(B) The overlap ratios of vasculatures labeled using Ultralabel/LEL-D649 and Ultralabel/CD31-A647 samples (n = 6 samples for each group).

(C) The signal-to-background ratios of vascular image stacks for each method (n = 9 samples for each labeling method).

(D) Fluorescence images of the vasculature of mouse brain slices casted by Ultralabel.

(E) Fluorescence images of the Ultralabel-casted blood vessels in mouse liver sections, showing the labeling effectiveness in both large and small blood vessels. All values are presented as the mean ± SD. Statistical significance in (C) (*, $p < 0.05$; ***, $p < 0.001$) was assessed using one-way ANOVA, followed by the Bonferroni *post hoc* test.

that of the other two methods tested, as shown in Figure 2C. Additionally, we imaged the blood vessels counterstained with common CD31 antibodies and DAPI at high magnification (20× and 40×), including large vessels and small capillaries (5–10 μm). As shown in Figure S1, the morphology of blood vessels displayed in a good manner, indicating Ultralabel did effectively label the true and complete vascular networks.

The Ultralabel technique demonstrated superior efficacy in uniformly labeling the vascular networks within different organs, both for large vessels and small capillaries. For example, Ultralabel displays complete and uniform labeling of vascular networks in the mouse brain (Figure 2D). In the mouse liver, the vasculature containing both large vessels and capillary networks can also be effectively identified (Figure 2E).

Ultralabel possesses superior tissue clearing compatibility with diverse existing tissue clearing methods

The fluorescence compatibility with major tissue clearing technologies poses another crucial factor in achieving fine reconstruction of the entire vascular network in different organs. Therefore, we then compared the tissue clearing compatibility of our protocol with other common labeling techniques. We selected five prevalent tissue clearing methodologies: organic solvent-based methods (uDISCO,[30] FDISCO,[31] PEGASOS[32]), hydrophilic solvent-based methods (CUBIC[33]), and hydrogel embedding-based methods (PACT[34]). Images of vascular information in mouse brain samples labeled by different methods were shown before and after clearing by each tissue clearing technique (Figure 3A). Signals labeled by Ultralabel were successfully preserved with no noticeable loss post-clearance by different protocols, as shown in Figure 3B.

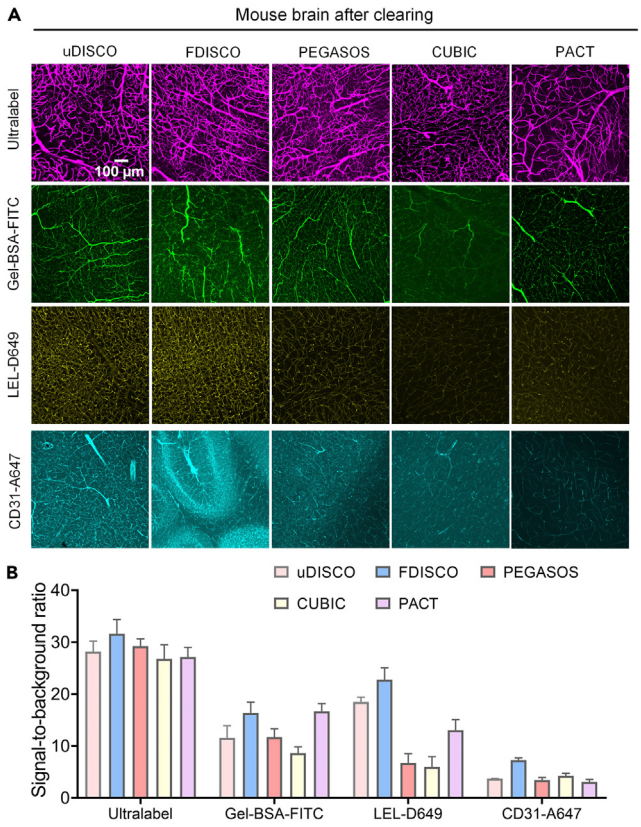

Figure 3. The Ultralabel method achieves labeling of vascular networks with robust compatibility

(A) Fluorescence images of vascular structures labeled by the four vascular labeling methods after clarification by indicated tissue clearing method.

(B) Quantification of the signal-to-background ratios of the labeled vascular structures after clearing with each method (n = 3 samples for each group).

However, the fluorescence signals labeled by other protocols were detrimentally lost after clearing to different extents. As a result, the signal-to-background ratios of vascular networks labeled by tested methods were obviously lower than those labeled by the Ultralabel protocol, especially after CUBIC clearing. Ultralabel protocol demonstrated the highest tissue clearing compatibility among all tested methods. We then tested whether Ultralabel could be used combined with common 3D immunolabeling protocol assisted by tissue clearing. Benefiting from the superiority in tissue clearing compatibility, the vascular signals labeled by Ultralabel could be preserved much better than those labeled by other methods after undergoing harsh treatment in the two major 3D immunolabeling procedures assisted by tissue clearing (Figure S2), indicating that Ultralabel is capable for simultaneous investigation of vascular networks together with other cell types in combination with diverse tissue clearing techniques and 3D immunolabeling. Additionally, we examined the Ultralabel-casted vessels before and after tissue clearing. As shown in Figure S3, the morphology of vascular networks casted by Ultralabel was maintained well after FDISCO clearing, showing no obvious collapse.

Ultralabel can be used for 3D visualization of diverse vascular networks combined with different optical clearing methods

To demonstrate the wide applicability of Ultralabel with tissue clearing technology, we combined Ultralabel with a wide range of tissue clearing methods to perform 3D reconstruction of diverse vascular structures. We labeled the entire architecture of brain vascular networks and then cleared the brain with PEGASOS, a solvent-based clearing method commonly used. As shown in Figure 4A and Video S1, the entire cerebral vascular structure could be finely visualized in 3D. The demonstration of the sagittal view in Figure 4B shows that all vascular structures were well captured throughout the imaging depth. The vascular networks in different brain regions, such as the cortex, hippocampus, and cerebellum, were also clearly identified (Figure 4C). The labeled mouse liver was cleared by FDISCO clearing method, and the liver vasculature was finely reconstructed (Figures 4D and 4E, Video S2). We also achieved three-color labeling of the neuron, vessels, and nucleus simultaneously visualized within the mouse spinal cord, which was assisted by the aqueous-based CUBIC clearing protocol (Figures 4F and 4G, Video S3). As shown in Figure 4H, the Ultralabel method enables high-resolution multi-channel labeling, with clear observations of nucleus, neurons, and blood vessels. In addition to soft tissue organs, the Ultralabel method is also capable for labeling the vascular networks within hard bones, including both large vessels and capillaries (Figures 4I and 4J). Therefore, the Ultralabel method can be used to obtain a complete 3D vascular network in both soft and hard tissues, combining multiple tissue clearing methods. The bright-field images of the Ultralabel-casted organs and bone before and after tissue clearing are shown in Figure S4.

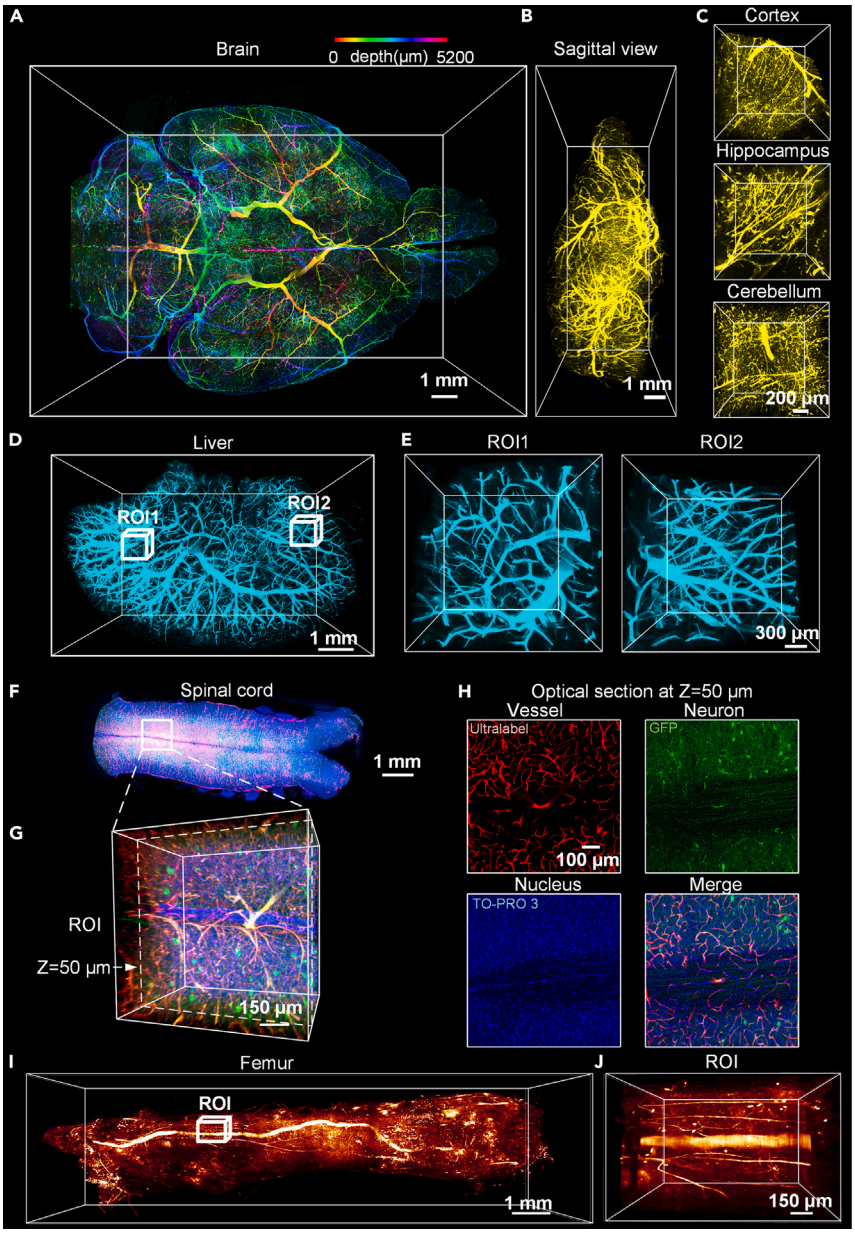

Figure 4. 3D reconstruction of vascular networks in typical organs using Ultralabel and different clearing methods

(A) 3D rendering of the Ultralabel-casted vascular network throughout an entire adult brain cleared with PEGASOS. Images along the z stack are colored by spectrum.

(B) The sagittal view of the reconstructed brain shown in (A).

(C) Detailed vasculature in the cortex, hippocampus, and cerebellum.

(D) 3D rendering of an Ultralabel-casted vascular network throughout an entire adult mouse liver cleared with FDISCO.

(E) Magnified views of the boxed regions in (D).

(F) 3D rendering of an Ultralabel-casted vascular network throughout the spinal cord of an adult Thy-1-GFP mouse cleared with CUBIC. Casted vessels are shown in red, GFP-expressing neurons in green, and labeled nucleus in blue.

(G) Magnified view of the boxed region in (F).

(H) The optical section of reconstructed images shown in (G) at Z = 50 μm imaging depth.

(I) 3D rendering of Ultralabel-casted vascular networks throughout an entire adult mouse femur cleared with FDISCO.

(J) Magnified views of the boxed regions in (I).

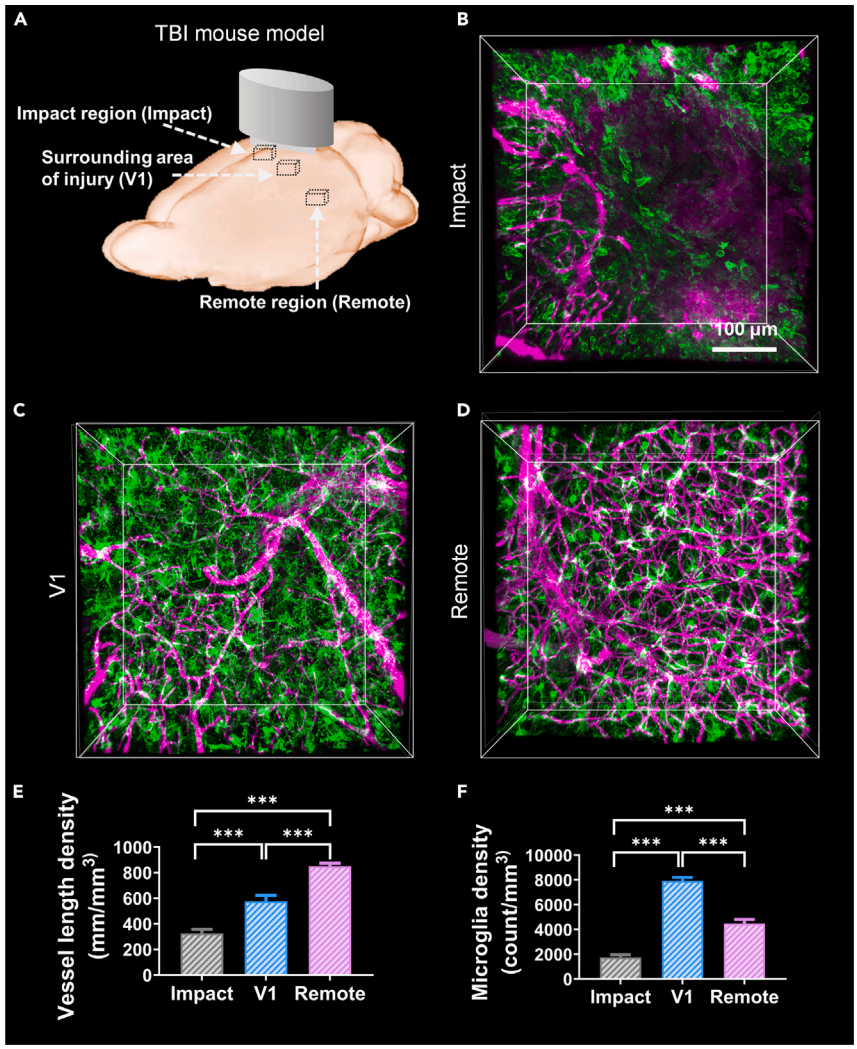

Figure 5. 3D visualization and analysis of vessel/microglia alteration in TBI mouse brain

(A) Experimental design for the TBI mouse model. The brain regions were defined as the impact region, the surrounding area of injury (V1), and the remote region.

(B) Magnification of impact region marked in (A). Casted vessels are shown in red and microglia in green.

(C) Magnification of the surrounding area of injury (V1) marked in (A).

(D) Magnification of remote region marked in (A).

(E) Quantification of vessel length density in the above three regions (n = 3 samples for each group).

(F) Quantification of microglia density in the above three regions (n = 3 samples for each group). All values are presented as the mean ± SD. Statistical significance in (e, f) (***, $p < 0.001$) was assessed using one-way ANOVA, followed by the Bonferroni *post hoc* test.

Ultralabel facilitates 3D investigation of vessel/microglia alteration in TBI mouse brain

The combination of vessel-labeling techniques with tissue clearing enables 3D visualization of vascular networks, thus allowing researchers to examine vascular alteration under pathological conditions. Given that the Ultralabel protocol possesses ideal vessel-labeling capability and superior compatibility for both tissue clearing and 3D immunolabeling, we applied Ultralabel in studying the microvascular remodeling and microglia alteration in traumatic brain injury (TBI) mouse brains (Figure 5A).

As expected, Ultralabel enabled simultaneous visualization of the vascular networks/microglia in TBI mouse brain tissue assisted by tissue clearing and immunolabeling. Magnifications of 3D rendering images were shown in three regions post-TBI, impact site, surrounding area of injury (primary visual cortex [V1]), and remote region (Figures 5B–5D), which revealed substantial loss of vascular structures in the injured region, as well as microglia gathering and activation in the area surrounding the injury. The quantitative analysis showed that the vessel length density and microglia density decreased obviously in injured regions, with microglia aggregation toward the damaged area via V1 (Figure 5E). These results suggested that Ultralabel could facilitate the studying of microvascular remodeling under specific pathological conditions.

DISCUSSION

The breakthroughs in fluorescence labeling and tissue clearing technology offer reliable tools for obtaining 3D vascular structures under specific physiological and pathological statuses. The fine labeling of vascular networks is the foundation for visualizing detailed vascular structural information in 3D form. In this study, we developed Ultralabel, a method with both robust vessel-labeling capability and excellent tissue clearing compatibility, enabling high-quality reconstruction of vascular networks within different organs. This method is based on a dextran dye with lysine cross-linking, which has bright fluorescence and a special fixation mechanism that can be stably fixed on biological tissues through aldehyde mediation. Labeling the vasculature with such a dye solution could achieve complete labeling of the vascular network with high signal-to-background ratio and strong tissue clearing compatibility. Using Ultralabel together with different tissue clearing techniques, we obtained high-quality vascular maps for diverse organs, and even for 3-color reconstruction within the mouse spinal cord.

The quality of vessel labeling and its compatibility with tissue clearing methods codetermine the imaging quality in optical tomography. Conventional immunolabeling requires a rather long time for passive diffusion of vessel-specific antibodies and usually achieves limited diffusion depth on large tissue. The method using injection via tail vein has overcome the problem for a long time but often leads to incomplete labeling for large vessels and weak signals, which is difficult to resolve. Therefore, filling the blood vessels with fluorescent dyes has become popular, which was pioneered by Tsai et al. since 2009.[25] The used filling dyes also varied, such as 1,1′-dioctadecyl-3,3,3′3′-tetramethylindocarbocyanine perchlorate (DiI),[35] Gel-BSA-FITC,[24] and Rhodamine isothiocyanate (RITC)-Dex-Glycidyl methacrylate (GMA) hydrogels.[26] However, DiI suffers from dye leakage and insufficient tissue clearing compatibility. RITC-Dex-GMA hydrogels partially resolved these problems but created higher barriers to entry. Gel-BSA-FITC could achieve better labeling performance and has been used in many studies,[16,24,25,28,29] but the inadequate tissue clearing compatibility for typical tissue clearing methods (e.g., CUBIC) and restricted access in some countries (e.g., China) prevent its wide use. Due to the availability of numerous vascular labeling methods and tissue optical clearing techniques for complex tissues, it can be challenging to identify a suitable pipeline for a specific application, as many factors must be considered. Table S1 summarizes the 3 types of strategies available for labeling the entire vascular network and their applicable tissue optical clearing techniques, along with their respective advantages and limitations. Advanced genetic labeling techniques offer reliable and bright fluorescence for vascular labeling at the capillary level. However, these techniques are time-consuming and technically challenging. It is also difficult to apply genetic manipulation to primates or humans. Endothelial-specific markers have effective labeling of true vascular networks, especially for small capillaries, but somewhat expensive and time-consuming for sufficient antibody penetration. It is less effective for large vessels, especially when labeling via vein injection. Fluorescent dye-filling techniques provide uniform and complete labeling for both large vessels and capillaries. However, some of these techniques may result in potential dye leakage, and certain methods may not be compatible with current tissue clearing techniques.[36] Here, we selected a special kind of dextran dye fused with lysine residue instead and developed Ultralabel. Similar with FITC-albumin, the dextran tracers will not only bind to the nearby endothelial cells via aldehyde-mediated fixation but also are stably entrapped in the hydrogel matrix during the vessel labeling, providing excellent vessel-labeling performance within different organs. Additionally, the lysine-fixable dextran is much easier to purchase from the worldwide Thermo Fisher Scientific company without restriction. More importantly, Ultralabel outperforms Gel-BSA-FITC due to its superior compatibility with most tissue clearing methods currently available, making it an ideal candidate for use alongside tissue clearing and 3D immunolabeling techniques. This simple innovation successfully solves the major problems associated with currently used fluorescent vascular labeling methods. Therefore, Ultralabel is more flexible for researchers to design their experiments for vascular imaging and analysis.

The development of various tissue clearing methods has provided an important means for the 3D imaging of mouse tissues. However, there are still significant differences in the structure and function of tissues/organs between rodents and humans.[37,38] This is why more and more researchers are using large, high-level animals for their research, such as pigs and macaques that share greater similarities with humans.[37,39–41] Tissue clearing methods have been developed for large volume samples, such as small-micelle-mediated human organ efficient clearing and labeling (SHANEL),[42] entangled link-augmented stretchable tissue-hydrogel (ELAST),[43] etc. However, complete labeling of blood vessels in larger animals remains a challenging task.[44,45] Filling blood vessels with fluorescent dyes via cardiac perfusion is currently an ideal labeling strategy for labeling large-volume animals. In addition to conventional vessel labeling, immunolabeling is also a powerful tool to label different cell types and structural information with antibodies, and 3D immunolabeling techniques have been developed along with tissue clearing in recent years. However, it is still difficult to combine vessel labeling with 3D immunolabeling for simultaneous visualization of cell type information and blood vessels, mainly due to the poor tissue clearing compatibility of current vessel-labeling methods. Moreover, larger tissues need to undergo longer and more rigorous tissue clearing procedures, making the tissue clearing compatibility of a vascular labeling method particularly important. By verifying the robust tissue clearing compatibility of our method with various optical tissue clearing protocols, it can be concluded that Ultralabel has great potential in vascular labeling for large-volume animals. Given that the developed Ultralabel protocol possesses unique advantages in tissue clearing compatibility, it is also expected to be used combined with 3D immunolabeling for the investigation of the relationship and interaction between different biological components and blood vessels.

It is worth noting that we have different protocols for different organs. For the labeling of the brain, distilled water is used to dissolve gelatin, while, for visceral organs, phosphate buffer saline (PBS) solution is used for dissolution. This is because, when using distilled water as a solvent to label blood vessels throughout the body of mice, blood vessels in the brain can be completely labeled, while blood vessels in visceral organs may experience dye leakage. We speculate that it is probably due to the existence of blood-brain barrier in the brain, which can effectively prevent dye leakage. Due to the higher salt balance of the PBS solution, the PBS-dissolved gelatin solution is more suitable for labeling the blood vessels of visceral organs. Actually, some vessel-labeling methods fail to label bone marrow organization due to poor circulation. However, the Ultralabel protocol is effective in labeling vascular networks at the capillary level within bones, such as the mouse femur.

In summary, we have established a method for vascular labeling that offers robust labeling capability and potent tissue clearing capability. This novel approach ensures the preservation of bright fluorescence, even during stringent and extended tissue clearing procedures. Designated as "Ultralabel," this method is not only efficient and user-friendly, but also practical for tracking and reconstructing vascular networks across various organs. Consequently, Ultralabel is projected to emerge as a powerful instrument for the appraisal of vascular structure in models of pathological diseases.

Limitations of the study

This study, while thorough, presents a few conceivable limitations that should be acknowledged. Due to the fact that existing tissue clearing methods are roughly divided into three categories, we have selected representative tissue clearing methods from the three categories to demonstrate Ultralabel's tissue clearing compatibility. Our study does not cover all existing methods, but we believe that Ultralabel has the potential to be compatible with most tissue clearing methods. The secondary concern relates to the use of pig skin gelatin as the hydrogel base due to its accessibility and user-friendly operation. While this choice was made for accessibility and ease of operation, it is important to recognize that gelatin's morphology is sensitive to temperature fluctuations. This temperature sensitivity renders the labeling procedure highly reliant on the ambient temperature, potentially complicating experimentation and compromising the integrity of labeling in colder laboratory environments. It is worth noting that gelatin can be replaced with alternative hydrogel bases under different conditions to suit specific experimental requirements.

STAR★METHODS

Detailed methods are provided in the online version of this paper and include the following:

- KEY RESOURCES TABLE
- RESOURCE AVAILABILITY
  - Lead contact
  - Materials availability
  - Data and code availability
- EXPERIMENTAL MODEL AND STUDY PARTICIPANT DETAILS
  - Animals
  - TBI mouse models
- METHOD DETAILS
  - Vascular labeling
  - Tissue clearing protocols
  - Immunolabeling
  - Imaging
  - Image data processing
- QUANTIFICATIONS AND STATISTICAL ANALYSIS
  - The signal-to-background ratio
  - The vessel length density
  - The microglia density
  - Statistical analysis

SUPPLEMENTAL INFORMATION

Supplemental information can be found online at https://doi.org/10.1016/j.isci.2024.109730.

ACKNOWLEDGMENTS

This study was supported by the National Natural Science Foundation of China (grant nos. 61860206009, 62375096, 82361138569, 82372012, 62105113), China Postdoctoral Science Foundation-funded project (grant nos. BX20200138 and 2021M691145), and the Open Competition Project of Wuhan East Lake High-tech Development Zone (grant no. 2023KJB224). We also thank the Optical Bio-imaging Core Facility of WNLO-HUST for their assistance with data acquisition.

AUTHOR CONTRIBUTIONS

Y.D., J.Z., and T.Y. designed the study. Y.D. and J.Z. designed and performed most of the experiments. Y.D. contributed to animal preparation. Y.D., X.L., and J.D. contributed to the vessel labeling of samples. Y.D. contributed to data analysis. Y.D. and J.Z. prepared the figures and wrote the manuscript. D.Z. and T.Y. supervised the project and revised the manuscript.

DECLARATION OF INTERESTS

The authors declare no competing interests.

Received: November 15, 2023
Revised: February 23, 2024
Accepted: April 9, 2024
Published: April 11, 2024

REFERENCES

1. Ribeiro, A.S.F., Zerolo, B.E., López-Espuela, F., Sánchez, R., and Fernandes, V.S. (2023). Cardiac System during the Aging Process. Aging Dis. *14*, 1105–1122. https://doi.org/10.14336/AD.2023.0115.
2. Toledo, A.G., Golden, G., Campos, A.R., Cuello, H., Sorrentino, J., Lewis, N., Varki, N., Nizet, V., Smith, J.W., and Esko, J.D. (2019). Proteomic atlas of organ vasculopathies triggered by Staphylococcus aureus sepsis. Nat. Commun. *10*, 4656. https://doi.org/10.1038/s41467-019-12672-x.
3. Tian, L., Goldstein, A., Wang, H., Ching Lo, H., Sun Kim, I., Welte, T., Sheng, K., Dobrolecki, L.E., Zhang, X., Putluri, N., et al. (2017). Mutual regulation of tumour vessel normalization and immunostimulatory reprogramming. Nature *544*, 250–254. https://doi.org/10.1038/nature21724.
4. Ganss, R. (2017). Tumour vessel normalization and immune checkpoint blockade: a new synergism. Immunol. Cell Biol. *95*, 497–498. https://doi.org/10.1038/icb.2017.30.
5. Zhao, L.R., and Willing, A. (2018). Enhancing endogenous capacity to repair a stroke-damaged brain: An evolving field for stroke research. Prog. Neurobiol. *163–164*, 5–26. https://doi.org/10.1016/j.pneurobio.2018.01.004.
6. Shichita, T., Ooboshi, H., and Yoshimura, A. (2023). Neuroimmune mechanisms and therapies mediating post-ischaemic brain injury and repair. Nat. Rev. Neurosci. *24*, 299–312. https://doi.org/10.1038/s41583-023-00690-0.
7. Gifre-Renom, L., and Jones, E.A.V. (2021). Vessel Enlargement in Development and Pathophysiology. Front. Physiol. *12*, 639645. https://doi.org/10.3389/fphys.2021.639645.
8. Hussain, S., Mubeen, I., Ullah, N., Shah, S.S.U.D., Khan, B.A., Zahoor, M., Ullah, R., Khan, F.A., and Sultan, M.A. (2022). Modern Diagnostic Imaging Technique Applications and Risk Factors in the Medical Field: A Review. BioMed Res. Int. *2022*, 5164970. https://doi.org/10.1155/2022/5164970.
9. Wen, X., Tuchin, V.V., Luo, Q., and Zhu, D. (2009). Controling the scattering of intralipid by using optical clearing agents. Phys. Med. Biol. *54*, 6917–6930. https://doi.org/10.1088/0031-9155/54/22/011.
10. Dodt, H.U., Leischner, U., Jährling, N., Jährling, N., Mauch, C.P., Deininger, K., Deussing, J.M., Zieglgänsberger, W., Zieglgänsberger, W., and Becker, K. (2007). Ultramicroscopy: three-dimensional visualization of neuronal networks in the whole mouse brain. Nat. Methods *4*, 331–336. https://doi.org/10.1038/nmeth1036.
11. Ertürk A, B.K., Jährling, N., Mauch, C.P., Hojer, C.D., Egen, J.G., Hellal, F., Bradke, F., Sheng, M., and Dodt, H.U. (2012). Three-dimensional imaging of solvent-cleared organs using 3DISCO. Nat. Protoc. *7*, 1983–1995. https://doi.org/10.1038/nprot.2012.119.
12. Renier, N., Wu, Z., Simon, D.J., Yang, J., Ariel, P., and Tessier-Lavigne, M. (2014). iDISCO: A Simple, Rapid Method to Immunolabel Large Tissue Samples for Volume Imaging. Cell *159*, 896–910. https://doi.org/10.1016/j.cell.2014.10.010.
13. Yang, B., Treweek, J.B., Kulkarni, R.P., Deverman, B.E., Chen, C.K., Lubeck, E., Shah, S., Cai, L., and Gradinaru, V. (2014). Single-Cell Phenotyping within Transparent Intact Tissue through Whole-Body Clearing. Cell *158*, 945–958. https://doi.org/10.1016/j.cell.2014.07.017.
14. Susaki, E.A., Ueda, H.R., Tainaka, K., Perrin, D., Kishino, F., Tawara, T., Watanabe, T.M., Yokoyama, C., Onoe, H., Eguchi, M., et al. (2014). Whole-Brain Imaging with Single-Cell Resolution Using Chemical Cocktails and Computational Analysis. Cell *157*, 726–739. https://doi.org/10.1016/j.cell.2014.03.042.
15. Lugo-Hernandez, E., Squire, A., Hagemann, N., Brenzel, A., Sardari, M., Schlechter, J., Sanchez-Mendoza, E.H., Gunzer, M., Faissner, A., and Hermann, D.M. (2017). 3D visualization and quantification of microvessels in the whole ischemic mouse brain using solvent-based clearing and light sheet microscopy. J. Cerebr. Blood Flow Metabol. *37*, 3355–3367. https://doi.org/10.1177/0271678X17698970.
16. Mohamud Yusuf, A., Hagemann, N., Schulten, S., Rausch, O., Wagner, K., Hussner, T., Qi, Y., Totzeck, M., Kleinschnitz, C., Squire, A., et al. (2020). Light Sheet Microscopy Using FITC-Albumin Followed by Immunohistochemistry of the Same Rehydrated Brains Reveals Ischemic Brain Injury and Early Microvascular Remodeling. Front. Cell. Neurosci. *14*, 625513. https://doi.org/10.3389/fncel.2020.625513.
17. Lee, E.J., Hong, S.K., Choi, D.H., Gum, S.I., Hwang, M.Y., Kim, D.S., Oh, J.W., and Lee, E.S. (2022). Three-dimensional visualization of cerebral blood vessels and neural changes in thick ischemic rat brain slices using tissue clearing. Sci. Rep. *12*, 15897. https://doi.org/10.1038/s41598-022-19575-w.
18. Todorov, M.I., Paetzold, J.C., Schoppe, O., Tetteh, G., Shit, S., Todorov-Völgyi, K., Todorov-Völgyi, K., Düring, M., Dichgans, M., Piraud, M., et al. (2020). Machine learning analysis of whole mouse brain vasculature. Nat. Methods *17*, 442–449. https://doi.org/10.1038/s41592-020-0792-1.
19. Jinyoung, S., Minjin, C., and Sung-Yon, K. (2016). Clearing and Labeling Techniques for Large-Scale Biological Tissues. Mol. Cell *39*, 439–446. https://doi.org/10.14348/molcells.2016.0088.
20. Renier, N., Wu, Z., Simon, D.J., Yang, J., Ariel, P., and Tessier-Lavigne, M. (2014). iDISCO: a simple, rapid method to immunolabel large tissue samples for volume imaging. Cell *159*, 896–910. https://doi.org/10.1016/j.cell.2014.10.010.
21. Kirst, C., Skriabine, S., Vieites-Prado, A., Topilko, T., Bertin, P., Gerschenfeld, G., Verny, F., Topilko, P., Michalski, N., Tessier-Lavigne, M., and Renier, N. (2020). Mapping the Fine-Scale Organization and Plasticity of the Brain Vasculature. Cell *180*, 780–795.e25. https://doi.org/10.1016/j.cell.2020.01.028.
22. Zhu, J., Liu, X., Deng, Y., Li, D., Yu, T., and Zhu, D. (2021). Tissue optical clearing for 3D visualization of vascular networks: A review. Vasc. Pharmacol. *141*, 106905. https://doi.org/10.1016/j.vph.2021.106905.
23. Robertson, R.T., Levine, S.T., Haynes, S.M., Gutierrez, P., Baratta, J.L., Tan, Z., and Longmuir, K.J. (2015). Use of labeled tomato lectin for imaging vasculature structures. Histochem. Cell Biol. *143*, 225–234. https://doi.org/10.1007/s00418-014-1301-3.
24. Di Giovanna, A.P., Tibo, A., Silvestri, L., Müllenbroich, M.C., Costantini, I., Allegra Mascaro, A.L., Sacconi, L., Frasconi, P., and Pavone, F.S. (2018). Whole-Brain Vasculature Reconstruction at the Single Capillary Level. Sci. Rep. *8*, 12573. https://doi.org/10.1038/s41598-018-30533-3.
25. Tsai, P.S., Kaufhold, J.P., Blinder, P., Friedman, B., Drew, P.J., Karten, H.J., Lyden, P.D., and Kleinfeld, D. (2009). Correlations of Neuronal and Microvascular Densities in Murine Cortex Revealed by Direct Counting and Colocalization of Nuclei and Vessels. J. Neurosci. *29*, 14553–14570. https://doi.org/10.1523/jneurosci.3287-09.2009.
26. Miyawaki, T., Morikawa, S., Susaki, E.A., Nakashima, A., Takeuchi, H., Yamaguchi, S., Ueda, H.R., and Ikegaya, Y. (2020). Visualization and molecular characterization of whole-brain vascular networks with capillary resolution. Nat. Commun. *11*, 1104. https://doi.org/10.1038/s41467-020-14786-z.
27. Xie, W., Gong, X.T., Cheng, X., Cao, J., Zhao, J., Zhang, H.L., and Zhang, S. (2021). LIMPID: a versatile method for visualization of brain vascular networks. Biomater. Sci. *9*, 2658–2669. https://doi.org/10.1039/d0bm01817a.
28. Spangenberg, P., Hagemann, N., Squire, A., Förster, N., Krauß, S.D., Qi, Y., Mohamud Yusuf, A., Wang, J., Grüneboom, A., Kowitz, L., et al. (2023). Rapid and fully automated blood vasculature analysis in 3D light-sheet image volumes of different organs. Cell Rep. Methods *3*, 100436. https://doi.org/10.1016/j.crmeth.2023.100436.
29. Olianti, C., Costantini, I., Giardini, F., Lazzeri, E., Crocini, C., Ferrantini, C., Pavone, F.S., Camici, P.G., and Sacconi, L. (2020). 3D imaging and morphometry of the heart capillary system in spontaneously hypertensive rats and normotensive controls. Sci. Rep. *10*, 14276. https://doi.org/10.1038/s41598-020-71174-9.
30. Pan, C., Cai, R., Quacquarelli, F.P., Ghasemigharagoz, A., Lourbopoulos, A., Matryba, P., Plesnila, N., Dichgans, M., Ertürk, A., and Ertürk, A. (2016). Shrinkage-mediated imaging of entire organs and organisms using uDISCO. Nat. Methods *13*, 859–867. https://doi.org/10.1038/nmeth.3964.
31. Qi, Y., Yu, T., Xu, J., Wan, P., Ma, Y., Zhu, J., Li, Y., Gong, H., Luo, Q., and Zhu, D. (2019). FDISCO: Advanced solvent-based clearing method for imaging whole organs. Sci. Adv. *5*, eaau8355. https://doi.org/10.1126/sciadv.aau8355.
32. Jing, D., Zhang, S., Luo, W., Gao, X., Men, Y., Ma, C., Liu, X., Yi, Y., Bugde, A., Zhou, B.O.,

et al. (2018). Tissue clearing of both hard and soft tissue organs with the PEGASOS method. Cell Res. *28*, 803–818. https://doi.org/10.1038/s41422-018-0049-z.

33. Tainaka, K., Murakami, T.C., Susaki, E.A., Shimizu, C., Saito, R., Takahashi, K., Hayashi-Takagi, A., Sekiya, H., Arima, Y., Nojima, S., et al. (2018). Chemical Landscape for Tissue Clearing Based on Hydrophilic Reagents. Cell Rep. *24*, 2196–2210.e9. https://doi.org/10.1016/j.celrep.2018.07.056.
34. Treweek, J.B., Chan, K.Y., Flytzanis, N.C., Yang, B., Deverman, B.E., Greenbaum, A., Lignell, A., Xiao, C., Cai, L., Ladinsky, M.S., et al. (2015). Whole-body tissue stabilization and selective extractions via tissue-hydrogel hybrids for high-resolution intact circuit mapping and phenotyping. Nat. Protoc. *10*, 1860–1896. https://doi.org/10.1038/nprot.2015.122.
35. Li, Y., Song, Y., Zhao, L., Gaidosh, G., Laties, A.M., and Wen, R. (2008). Direct labeling and visualization of blood vessels with lipophilic carbocyanine dye DiI. Nat. Protoc. *3*, 1703–1708. https://doi.org/10.1038/nprot.2008.172.
36. Zhu, J., Deng, Y., Yu, T., Liu, X., Li, D., and Zhu, D. (2022). Optimal combinations of fluorescent vessel labeling and tissue clearing methods for three-dimensional visualization of vasculature. Neurophotonics *9*, 045008. https://doi.org/10.1117/1.NPh.9.4.045008.
37. Pabst, R. (2020). The pig as a model for immunology research. Cell Tissue Res. *380*, 287–304. https://doi.org/10.1007/s00441-020-03206-9.
38. Huang, M., Yang, J., Li, P., and Chen, Y.; Embryo-Engineered Nonhuman Primate Models: Progress and Gap to Translational Medicine (2021). Embryo-Engineered Nonhuman Primate Models: Progress and Gap to Translational Medicine. Research (Wash D C) *2021*, 9898769. https://doi.org/10.34133/2021/9898769.
39. Hou, N., Du, X., and Wu, S. (2022). Advances in pig models of human diseases. Animal Model. Exp. Med. *5*, 141–152. https://doi.org/10.1002/ame2.12223.
40. Neff, E.P. (2019). Cancer modeling thinks big with the pig. Lab. Anim *48*, 75–78. https://doi.org/10.1038/s41684-019-0246-5.
41. Palliyaguru, D.L., Shiroma, E.J., Nam, J.K., Duregon, E., Vieira Ligo Teixeira, C., Price, N.L., Bernier, M., Camandola, S., Vaughan, K.L., Colman, R.J., et al. (2021). Fasting blood glucose as a predictor of mortality: Lost in translation. Cell Metabol. *33*, 2189–2200.e3. https://doi.org/10.1016/j.cmet.2021.08.013.
42. Zhao, S., Todorov, M.I., Cai, R., Maskari, R.A., Steinke, H., Kemter, E., Mai, H., Rong, Z., Warmer, M., Stanic, K., et al. (2020). Cellular and Molecular Probing of Intact Human Organs. Cell *180*, 796–812.e19. https://doi.org/10.1016/j.cell.2020.01.030.
43. Ku, T., Guan, W., Evans, N.B., Sohn, C.H., Albanese, A., Kim, J.G., Frosch, M.P., and Chung, K. (2020). Elasticizing tissues for reversible shape transformation and accelerated molecular labeling. Nat. Methods *17*, 609–613. https://doi.org/10.1038/s41592-020-0823-y.
44. Xu, F., Shen, Y., Ding, L., Yang, C.-Y., Tan, H., Wang, H., Zhu, Q., Xu, R., Wu, F., Xiao, Y., et al. (2021). High-throughput mapping of a whole rhesus monkey brain at micrometer resolution. Nat. Biotechnol. *39*, 1521–1528. https://doi.org/10.1038/s41587-021-00986-5.
45. Costantini, I., Mazzamuto, G., Roffilli, M., Laurino, A., Maria Castelli, F., Neri, M., Lughi, G., Simonetto, A., Lazzeri, E., Pesce, L., et al. (2021). Large-scale, cell-resolution volumetric mapping allows layer-specific investigation of human brain cytoarchitecture. Biomed. Opt Express *12*, 3684–3699. https://doi.org/10.1364/BOE.415555.
46. Schindelin, J., Arganda-Carreras, I., Frise, E., Kaynig, V., Longair, M., Pietzsch, T., Preibisch, S., Rueden, C., Saalfeld, S., Schmid, B., et al. (2012). Fiji: an open-source platform for biological-image analysis. Nat. Methods *9*, 676–682. https://doi.org/10.1038/nmeth.2019.

STAR★METHODS

KEY RESOURCES TABLE

REAGENT or RESOURCE	SOURCE	IDENTIFIER
Antibodies		
Anti-CD31 Alexa Fluor 647	BioLegend	Cat#102416, RRID: AB_493410
Anti-GFAP antibody	Proteintech	Cat#16825-1-AP, RRID: AB_2109646
Goat anti-rabbit secondary antibody Alexa Fluor 488	Abcam	Cat#ab150077, RRID: AB_2630356
Goat anti-rabbit secondary antibody Alexa Fluor 647	Abcam	Cat#ab150083, RRID: AB_2714032
Anti- Iba1 antibody	Abcam	Cat# ab5076, RRID: AB_2224402
Chemicals, peptides, and recombinant proteins		
PBS	Sigma-Aldrich	Cat#P3813
Paraformaldehyde	Sigma-Aldrich	Cat#158127
Pork skin gelatin	Sigma-Aldrich	Cat# G1890
MeOH	Sinopharm Chemical Reagent Co. Ltd.	Cat#10014118
Tert-butanol	Sigma-Aldrich	Cat#360538
Tetrahydrofuran	Sinopharm Chemical Reagent Co., Ltd., Shanghai, China	Cat#40058161
DBE	Sigma-Aldrich	Cat#108014
Quadrol	Sigma-Aldrich	Cat#122262
PEGMMA500	Sigma-Aldrich	Cat#409529
Benzyl benzoate	Sigma-Aldrich	Cat#W213802
Benzyl alcohol	Sigma-Aldrich	Cat#24122
DPE	Sigma-Aldrich	Cat#P24101
EDTA	Sigma-Aldrich	Cat#324503
DL-alpha-tocopherol	Sigma-Aldrich	Cat#47786
Dichloromethane (DCM)	Sigma-Aldrich	Cat#270997
Sorbitol	Sigma-Aldrich	Cat#85529
Triton X-100	Sigma-Aldrich	Cat#T8787
N-butyl diethanolamine	Tokyo Chemical Industry	Cat#B0725
Antipyrine	Tokyo Chemical Industry	Cat#D1876
Nicotinamide	Tokyo Chemical Industry	Cat#N0078
VA-044	Wako Chemicals, Osaka, Japan	011–19365
Acrylamide	Sigma-Aldrich	Cat#A8887
DAPI	Thermo Fisher scientific	Cat#D1306
TO-PRO-3	Thermo Fisher scientific	Cat#T3605
DMSO	Sigma-Aldrich	Cat#T8418
Goat serum	Boster Bio	Cat#AR1009
Tween 20	Sigma-Aldrich	Cat#P9416
Dextran, tetramethylrhodamine, 3000 MW, anionic, lysine fixable	Thermo Fisher scientific	Cat#D3308
Dextran, tetramethylrhodamine, 10,000 MW, anionic, fixable	Thermo Fisher scientific	Cat#D1868

(*Continued on next page*)

Continued

REAGENT or RESOURCE	SOURCE	IDENTIFIER
Dextran, tetramethylrhodamine, 70,000 MW, lysine fixable	Thermo Fisher scientific	Cat#D1818
Dextran, tetramethylrhodamine, 2,000,000 MW, lysine fixable	Thermo Fisher scientific	Cat#D7139
DyLight 649-lectin	Vector Laboratories	Cat#DL1178
DyLight 594-lectin	Vector Laboratories	Cat#DL1177
BSA-FITC	Xi'an Ruixi Biological Technology Co., Ltd	Cat#R-FB-005
Experimental models: Organisms/strains		
C57BL/6J	Jackson Laboratories	Cat# JAX:000664, RRID:IMSR_JAX:000664
Software and algorithms		
MATLAB	Mathworks	https://www.mathworks.com/products/matlab.html
Imaris	Bitplane	https://www.bitplane.com/imaris/imaris
Fiji	Schindelin et al.[46]	https://imagej.nih.gov/ij/
Other		
Conical tubes (50 mL)	Corning	Cat#430828
Conical tubes (15 mL)	Corning	Cat#430790
Syringe pump	Leadfluid	Cat#TFD04
Peristaltic pump	Leadfluid	Cat#BT100L

RESOURCE AVAILABILITY

Lead contact

Further information and requests for resources and reagents should be directed to the lead contact, Dan Zhu (dawnzh@mail.hust.edu.cn).

Materials availability

All unique/stable reagents generated in this study are available from the lead contact without restriction. Further information and requests for resources and reagents should be directed to and will be fulfilled by the lead contact Prof. Dan Zhu (dawnzh@mail.hust.edu.cn).

Data and code availability

- Data: This paper does not report Standardized datatypes. All data reported in this paper will be shared by the lead contact upon request.
- Code: This paper does not report any original code.
- Any additional information necessary to reproduce results or reanalyze the data presented in this study will be made available upon request to the lead contact.

EXPERIMENTAL MODEL AND STUDY PARTICIPANT DETAILS

Animals

Wild mice (C57BL/6J, 8–12 weeks old, male) and Thy1-GFP-M mice (8–12 weeks old, male) were used in this study. All animals were housed on a 12 h light/dark cycle at 23 $\pm$ 1°C with free access to food and water in specific pathogen-free (SPF) cages. All animal experiments were performed under the Experimental Animal Management Ordinance of Hubei Province, P.R. China, and the guidelines from the Huazhong University of Science and Technology and were approved by the Institutional Animal Ethics Committee of Huazhong University of Science and Technology.

TBI mouse models

The mice were anesthetized with 5% isoflurane delivered in surgical grade air before the surgery and maintained at 2.5% isoflurane via nose cone. While anesthetized, body temperature was maintained using an isothermal heating pad. In preparation for the TBI procedure, anesthetized mice were placed in a stereotaxic frame. The injury was triggered via a controlled cortical impact device consisting of a fixed impactor using the following parameters: a tube diameter of 4 mm, impact speed of 1.5 m/s, and impact depth of 1 mm. The resulting injury was

obvious with these parameters. After surgery, the mice were recovered in a warmed holding cage and monitored until ambulatory. And then were housed on a 12 h light/dark cycle at 23 ± 1°C with free access to food and water in specific pathogen-free (SPF) cages. The mice were vascularly labeled and sampled after 3 days.

METHOD DETAILS

Vascular labeling

Ultralabel for vascular labeling

Mice were deeply anesthetized with a mixture of ketamine/xylazine thiazide (100/20 mg/kg) and then the heart was infused with 0.01M phosphate-buffered saline (PBS, no. P3813; Sigma-Aldrich) for blood washing. Gelatin solutions were prepared by dissolving porcine dermal gelatin (no. G1890; Sigma-Aldrich) in hot 0.01 M PBS or distilled water (the brain was marked for dissolution in water and the organs were marked for dissolution in 0.01 M PBS). The lysine-fixable dextran conjugated with tetramethylrhodamine (no. D1818; Thermo Fisher scientific) was dissolved in a 2% (w/v) gelatin solution at a concentration of 0.005% (w/v) and the mixed solution was kept at 40°C–45°C until infusion before use. Next, 10–15 mL of the mixture was infused under warm conditions. The perfused mouse body was then transferred to a low temperature environment (around 4°C) to rapidly cool and solidify the gelatin solution in the blood vessels. After cooling, the required mouse organs were extracted and fixed in 4% paraformaldehyde (PFA, Sigma-Aldrich, 158127) at 4°C overnight. Another version of lysine-fixable dextran with different molecular weights was also involved in this study for comparison, including 3 kDa (no. D3308; Thermo Fisher scientific), 10 kDa (no. D1868; Thermo Fisher scientific), 2000 kDa (no. D7139; Thermo Fisher scientific).

Gel-BSA-FITC for vascular labeling

We used the procedure described by Tsai et al. with slight modifications. Gelatin solutions were prepared by dissolving porcine dermal gelatin in hot 0.01 M PBS. BSA-FITC powder (no. R-FB-005, Xi'an Ruixi Biological Technology Co., Ltd) was dissolved in 2% (w/v) gelatin solution at a concentration of 0.5% (w/v) and the mixed solution was kept at 40°C–45°C before use. A mixture of ketamine/xylazine (100/20 mg/kg) was used to deeply anesthetize the mice, and then 0.01M PBS was infused into the heart to wash out the blood. Next, 10–15 mL of the mixture was infused under warm conditions. The perfused mouse body was then transferred to a low temperature environment (around 4°C) to rapidly cool and solidify the gelatin solution in the blood vessels. After cooling, the required mouse organs were extracted and fixed in 4% PFA at 4°C overnight.

Lectin and CD31 antibodies for vascular labeling

A DyLight 649 conjugated L. esculentum (Tomato) lectin (LEL-D649, no. DL-1178; Vector Laboratories), A DyLight 594 conjugated L. esculentum (Tomato) lectin (LEL-D594, no. DL-1177; Vector Laboratories) and an Alexa Fluor 647 conjugated anti-mouse CD31 antibody (CD31-A647, no. 102416, BioLegend) were also used to label the vasculature. Mice were deeply anesthetized with a mixture of ketamine/xylazine (100/20 mg/kg). LEL-D649 or LEL-D594 were diluted in saline to a concentration of 0.5 mg/mL and injected into the body of an anesthetized mouse via the tail vein (0.1 mL per mouse). Mice were deeply anesthetized with a mixture of ketamine/xylazine (100/20 mg/kg). Alexa Fluor 647 conjugated anti-mouse CD31 antibody was diluted in saline to a concentration of 0.075 mg/mL and injected into the anesthetized mouse body via the tail vein (0.2 mL per mouse). After injection, the animals were placed in a warm cage for 30 min before perfusion. After labeling and perfusion, the desired organs were excised from the animal bodies and post-fixed in 4% PFA at 4°C overnight. After injection, animals were placed in a warm cage for 30 min before perfusion. After labeling and perfusion, the desired organs were excised from the animal bodies and post-fixed in 4% PFA at 4°C overnight. The fixed tissues were sectioned using a commercially available vibrometer (Leica VT 1200s, Germany).

Tissue clearing protocols

We used different tissue clearing schemes based on organic solvents, including uDISCO, FDISCO, and PEGASOS; based on hydrophilic reagents, CUBIC; and the hydrogel embedding method, PACT. All evaluated digestion schemes were performed according to the instructions in the original publication. A brief summary of the clearing procedures for each method is given below.

uDISCO

Dehydration reagents were prepared by mixing pure tert-butanol (no. 10014118; Sigma-Aldrich) with distilled water at concentrations of 30%, 50%, 70%, 80%, 90%, 96%, and 100% (v/v). Fixed tissues were dehydrated sequentially in each reagent. The dehydrated tissue was then immersed in dichloromethane and BABB-D4; prepared by mixing BABB (benzyl alcohol + benzyl benzoate 1:2, no. 24122 and no. W213802; Sigma-Aldrich) with diphenyl ether (DPE) (no. P24101; Sigma-Aldrich) at a ratio of 4:1 and adding 0.4% vol DL-alpha-tocopherol (Vitamin E) (no. 47786; Sigma-Aldrich); until the sample became transparent. The time for each dehydration step (30%–100% tert-butanol) is 4 h (tissue section) and the time for matching RI with BABB-D4 is 4 h (tissue section). The dehydration step was performed at 35°C and the RI matching step was performed at room temperature with gentle shaking.

FDISCO

This method consists of two steps: dehydration and RI matching. First, a solution of tetrahydrofuran (THF) (no. 40058161; Sinopharm Chemical Reagent Co., Ltd., Shanghai, China) was used to dehydrate the fixed tissue in concentration gradients of 50%, 70%, 80%, and 100%. The pH of

each THF solution was adjusted to 9.0 by the addition of triethylamine. The dehydrated tissue was then incubated in pure dibenzyl ether (DBE) (no. 108014; Sigma-Aldrich) for RI matching. The time for each dehydration step (50%–100% THF) is 4 h (tissue section)/12 h (whole organ), and the time for RI matching with DBE is 4 h (tissue section)/12 h (whole organ). All steps were performed at 4°C with gentle shaking.

PEGASOS

The sample was first decolorized with a 25% Quadrol (no. 122262; Sigma-Aldrich) decolorization solution. The sample was then dehydrated in a gradient of tert-butanol solution, tB-PEG (70% (v/v) tert-butanol, 27% (v/v) PEG methacrylate Mn 500 (PEGMMA500) (no. 409529; Sigma-Aldrich) and 3% w/v Quadrol. The samples were then immersed in BB-PEG [75% (v/v) benzyl benzoate (BB) and 25% (v/v) PEGMMA500] with the addition of 3% (w/v) Quadrol for clearing. The time for decolorization is 12 h (tissue section)/24 h (whole organ), and the adaptation time between each dehydration step and the final RI is 4 h (tissue section)/12 h (whole organ). All steps were performed at 37°C with gentle shaking.

CUBIC

CUBIC-L is a mixture of 10% (w/w) N-butyl diethanolamine (no. B0725; Tokyo Chemical Industry) and 10% (w/w) Triton X-100 (no. T8787; Sigma-Aldrich) in distilled water. CUBIC-R was prepared by mixing 45% (w/w) antipyrine (no. D1876; Tokyo Chemical Industry) with 30% (w/w) nicotinamide (no. N0078; Tokyo Chemical Industry) in distilled water. The samples were incubated and degreased in CUBIC-L for 1.5 days (tissue section)/3 days (whole organ), washed with PBS for 6 h, and then exposed to CUBIC-R for RI matching for 12 h (tissue section)/2 days (whole organ). All steps were performed at 37°C with gentle shaking.

PACT

The PACT clearing method consists of three steps: hydrogel embedding, degreasing, and RI adjustment. First, the samples were incubated in A4P0 hydrogel solution (4% acrylamide (no. A8887; Sigma-Aldrich) in 0.01M PBS), incubated with VA-044(no. 011–19365; Wako Chemicals, Osaka, Japan) at 4°C overnight and incubated at 37°C for 6 h to achieve polymerization. The embedded sample was then washed with 0.01M PBS and degreased in 0.01M PBS containing 8% sodium dodecyl sulfate (SDS) (no. 30166480; Sinopharm Chemical Reagent Co., Ltd., Shanghai, China). The sample was washed again with PBS and immersed in a sorbitol-based refractive index matching solution (sRIMS) (75% (w/v) sorbitol solution) until the tissue became transparent. The SDS degreasing time is 96 h and the RI matching time is 24 h. All steps were performed at 37°C with gentle shaking.

Decalcification

For clearing hard tissue samples, 4% PFA fixation was performed at room temperature for 12 h and then samples were immersed in 20% EDTA (pH 7.0) at 37°C in a shaker for 4 days. Samples were then washed with H2O for at least 30 min to elute excessive EDTA (no. 324503; Sigma-Aldrich).

Immunolabeling

DAPI and TO-PRO 3

After washing with PBS, DAPI (1:1000, no. D1306; Thermo Fisher scientific) or TO-PRO 3 (1:2000, no. T3605; Thermo Fisher scientific) dye was added in PBS for 12 h (tissue section)/3 days (whole organ) at 37°C for cell nuclei staining.

Protocol 1 (hydrophilic)

Fixed brain slices were first pretreated with CUBIC-L solution for 2.5 days and then washed with PBS for 0.5 days. Pretreated samples were incubated in 0.2% PBST containing 20% DMSO (no. D8418; Sigma-Aldrich) and 0.3 M glycine at 37°C overnight, washed in 0.2% PBST containing 10% DMSO and 6% goat serum at 37°C for 12 h, washed in PTwH (PBS-0.2% Tween 20 (no. 409529; Sigma-Aldrich) with 10 mg/mL heparin) overnight and then incubated with Anti-GFAP antibody (1:500, no. 16825; Proteintech) dilutions in PTwH containing 5% DMSO, 3% goat serum and 0.01% (w/v) sodium azide at 37°C with gentle shaking on a shaker for 1 day. The sections were then washed in PTwH for 1 day and incubated with a secondary antibody (1:500) diluted in PTwH containing 3% goat serum (no. AR1009; Boster Bio) and 0.01% (w/v) sodium azide at 37°C with gentle shaking for 1 day. Then the sections were washed in PBS for 12 h (for 3D immunolabeling 1 day). Finally, exposed to CUBIC-R for RI matching for 12 h (tissue section)/2 days (whole organ). All steps were performed at 37°C with gentle shaking.

Protocol 2 (hydrophobic)

Fixed brain slices were first pretreated with a series of methanol (no. 10014118; Sinopharm Chemical Reagent Co. Ltd.)/DiH2O solutions: 20%, 40%, 60%, 80%, 100%, 80%, 60%, 40%, 20%, 1 h for each step (for 3D immunolabeling 3 h), then washed with PBS for 6 h. Pretreated samples were incubated in 0.2% PBST containing 20% DMSO and 0.3 M glycine at 37°C overnight, blocked in 0. 2% PBST containing 10% DMSO and 6% goat serum at 37°C for 12 h (for 3D immunolabeling 1 day), washed in PTwH (PBS-0.2% Tween 20 (no. P9416; Sigma-Aldrich) with 10 mg/mL heparin) overnight and then incubated with Anti-GFAP antibody (1:500) or Anti-Iba1 antibody (1:500, no. ab5076; Abcam) were in PTwH containing 5% DMSO, 3% goat serum and 0.01% (w/v) sodium azide at 37°C with gentle shaking on a shaker for 1 day (for 3D immunolabeling

3 days). Sections were then washed in PTwH for 1 day and incubated with secondary antibody (1:500) diluted in PTwH containing 3% goat serum and 0.01% (w/v) sodium azide at 37°C with gentle shaking for 1 day (for 3D immunolabeling 3 days). Then the sections were washed in PBS for 12 h (for 3D immunolabeling 1 day). The samples were shaken with a series of methanol/DiH2O solutions (20%, 40%, 60%, 80%, 100%, 100% v/v) at room temperature, followed by a DCM (no. 270997; Sigma-Aldrich). The dehydrated tissue was then incubated in pure dibenzyl ether (DBE) for RI matching. The time for each dehydration step is 4 h (tissue section)/12 h (whole organ), and the time for RI matching with DBE is 4 h (tissue section)/12 h (whole organ).

Imaging

The bright field images were taken with a digital camera. A light microscope (LiToneXL, Optical Innovation Technology, China) equipped with a 4× objective (NA = 0.28, working distance (WD) = 20 mm) is used to image dissected brains and other samples. The thin layer is illuminated from the four sides of the specimen and the merged image is stored. Laser scanning confocal microscope (LSM710, Zeiss, Germany) for imaging tissue sections; use 5× objective (NA = 0.25, WD = 12.5×mm), 10× objective (NA = 0.5, WD = 2×mm), 20× objective (NA = 0.8, WD = 0.55 mm). Data were collected using Zen 2011 SP2 software (version 8.0.0.273, Carl Zeiss GmbH, Germany).

Image data processing

All raw image data were acquired in lossless TIFF format (8-bit for confocal microscopy and 16-bit for light-sheet microscopy). Processing and 3D rendering were performed on a Dell workstation with an 8-core Xeon processor, 256 GB RAM, and an Nvidia Quadro P2000 graphics card. Imaris (version 7.6, Bitplane AG) and Fiji (version 1.51n) were used for 3D and 2D image visualization,[46] respectively. The 16-bit light sheet images were converted to 8-bit images by Fiji to allow fast processing by other software such as Imaris. Image stitching was performed as follows: The image acquired by the Zeiss confocal microscope and the LiToneXL light sheet microscope could be stitched automatically using the data acquisition software provided by the company. If manual stitching was required, we recommended the use of the 'Grid/Collection stitching' plug-in in Fiji. Briefly, the 'Grid: column-by-column' mode was selected and the stitching order was determined by the data acquisition mode (we used Down & Right). Then the parameters such as grid size, tile overlap value, and input and output file directories were set manually based on the image data. Then the plugin would run and stitch the data with the selected parameters.

QUANTIFICATIONS AND STATISTICAL ANALYSIS

The signal-to-background ratio

To evaluate the efficiency of different container labeling methods and the fluorescence compatibility of each vessel labeling technique with different clearing procedures, the signal-to-background ratio was calculated. First, the image stack (50 μm thickness) is imported into ImageJ. The 'threshold' function in ImageJ is used to extract vascular signals for each image in the image stack. The function calculates the average signal strength for each image. Next, three areas without blood vessels are manually selected as the background area for each image in the image stack. The average signal intensity of these areas is taken as the background intensity of each image. The signal-to-background ratio of each image in the stack is defined as the average signal intensity divided by the average background intensity.

The vessel length density

3D vascular reconstruction and quantification by Imaris was performed using the pipeline described in previous studies. In brief, the "Threshold (loops)" algorithm in the filament module was used to trace and quantify blood vessels. The parameter for the filament diameter was automatically set by the algorithm according to the voxel size. The threshold for extracting vascular information was manually adjusted to ensure the complete recognition of all blood vessels. After reconstruction of the vascular network, the local vessel density, average radius, and vessel segment length were obtained using the "statistics-selection" in the filament module.

The microglia density

Fluorescent images of brain regions were analyzed with Imaris software. Automated calculations and segmentation were adjusted manually to incorporate unrecognized signal points.

Statistical analysis

Data are presented as the mean ± SD and were analyzed using SPSS software (Version 22, IBM, USA) with a 95% confidence interval. Sample sizes are given in the figure legends. For the analysis of statistical significance, the normality of the data distribution in each experiment was checked using the Shapiro-Wilk test. The homogeneity of variance for each group was assessed using Levene's test. p values were calculated using one-way ANOVA followed by the Bonferroni post hoc test to compare data in Figures 1C, 1D, 2B, 5E, and 5F. In this study, $p < 0.05$ was considered significant (*, $p < 0.05$; **, $p < 0.01$; ***, $p < 0.001$).